Buckling and Strength of Cold-Formed Thin-Walled Built-Up Columns under Axial Compression: Tests and Code Evaluation

Fei Yang[1,*], Xingkui Yang[2]

[1] Shanxi Polytechnic College, Shaanxi, China

[2] Shanxi No. 6 Construction Group Co., Ltd., Shaanxi, China

Received 03 November 2025; received in revised form 30 December 2025; accepted 02 January 2026

DOI: https://doi.org/10.46604/ijeti.2026.15850

Abstract

This study examines the axial-compression behaviour of cold-formed thin-walled steel built-up columns. Sixty concentric axial tests are carried out on six cross-section configurations (single C- and U-sections and four screw-fastened built-up sections) with lengths from 500 to 3000 mm. The measured capacities are compared with predictions from the Chinese code GB 50018-2002 using the Effective Width Method (EWM) and from AISI S100-2007 using both EWM and the Direct Strength Method (DSM). For closed multi-limb built-up sections, members with slenderness $\lambda < 70$ failed mainly by local buckling, whereas $\lambda > 70$ led to global buckling. For open built-up sections, $\lambda < 80$ is governed by distortional buckling and $\lambda > 80$ by global buckling. Overall, GB EWM provided the closest strength predictions for the built-up members, while AISI DSM is generally conservative. The results offer practical guidance for the design of cold-formed steel built-up compression members.

Keywords: cold-formed thin-walled steel, built-up sections, axial compressive capacity, design methods

1. Introduction

Cold-formed steel (CFS) built-up columns, composed of multiple thin-walled elements connected by screws, have become widely adopted as primary load-bearing members in modern light-gauge steel structures due to their high strength-to-weight ratio and cost-efficiency[1]. These built-up sections (which can form closed box sections or open back-to-back sections) offer enhanced axial capacity compared to individual channel members, and are increasingly used in mid- to high-rise cold-formed steel buildings. However, the assembly of several plate elements into one column leads to complex buckling behavior. Depending on the cross-section and member slenderness, built-up columns may exhibit local plate buckling, distortional (stiffener-related) buckling, overall (global) Euler buckling, or combinations of these modes [2]. Recent studies have confirmed that interactive buckling modes (e.g. local–distortional or local–global interactions) frequently govern the strength of CFS built-up members [3], posing challenges for both analysis and design.

Traditional design standards did not originally provide explicit methods for multi-limb built-up CFS columns. For instance, the North American and Australasian specifications have historically treated back-to-back built-up columns by using a modified slenderness approach to account for connector spacing, rather than a dedicated design formula [4]. This simplified approach can be unreliable because it does not fully capture the partial composite action and buckling mode interactions between the connected elements. As a result, there has been a surge of international research in recent years to understand the buckling mechanisms of built-up CFS columns and to develop suitable design methods.

* Corresponding author. E-mail address: sxzyjsxyyf@126.com

Numerous experimental and numerical studies have been carried out on CFS built-up columns under axial compression. For closed cross-sections (e.g., box sections assembled from four C-channels), extensive test data and analytical models have been reported. Nie et al. (2022) proposed design formulas for box columns composed of four channels [2], while Selvaraj and Madhavan (2023) evaluated the influence of slenderness and fastener spacing and assessed DSM/EWM design predictions, highlighting the critical role of connector spacing and the need to refine design curves when mode interaction occurs [1].

Innovative built-up configurations and open built-up sections have also been investigated. Deepak and Ananthi (2021) examined a novel "double-I box" section using tests and FE analysis, reporting its buckling behavior and axial strength [3]. For back-to-back open channels, Zhang et al. (2023) studied the effects of web perforations and edge stiffeners [5], and Zhou et al. (2022) showed that existing standards can be inadequate for slender columns with local–global interaction, proposing improved DSM equations [6].

Studies on atypical built-up forms (e.g., three-limb and multi-limb hybrid sections) further elucidate buckling behavior and strength, forming an important database for developing and calibrating design methods. Recent work has also underscored the influence of intermediate/web stiffeners and connection detailing on the axial response of both open and closed built-up members, with direct implications for the applicability and accuracy of DSM and EWM formulations [7–12].

A consistent theme in recent literature is that conventional design approaches (EWM and DSM, codified for single sections) do not always predict the capacity of built-up columns accurately. For aluminum alloy members, studies on screw-fastened back-to-back channel columns and extruded SHS/T-section columns show that axial strength is strongly affected by local–distortional–global buckling interaction and connection details (e.g., screw spacing, web openings), so direct adoption of steel rules can lead to inaccurate resistance predictions and requires modified slenderness limits and resistance factors for aluminum built-up members [13]. These discrepancies have motivated several enhancements: Selvaraj and Madhavan (2022) introduced an improved DSM including fastener spacing via a modified slenderness factor [1]. Li et al. (2024) examined failure mechanisms and reliability of CFS built-up columns governed by distortional buckling, providing data for calibrating safety margins and advancing more accurate, mode-aware design methods [6].

Cold-formed stainless steel built-up columns have attracted increasing attention in durability-critical applications, with tests on T-/cruciform sections and back-to-back channels revealing significant post-yield reserve, strong local–global buckling interaction, and stress–strain behavior distinct from carbon steel, so DSM/EWM provisions calibrated for CFS can be either overly conservative or unconservative, motivating material-specific design procedures. Despite extensive work on CFS-built-up columns, important design gaps remain for complex multi-limb members [1–6]. Existing databases focus mainly on conventional box sections and back-to-back channels, while systematic tests on hybrid C–U multi-limb configurations (CU, C2U2, C3U) with matching single-limb baselines are still limited [1–3, 5–6]. Moreover, most studies benchmark only North American/Australasian DSM/EWM provisions, with scarce cross-code evaluation including the Chinese GB 50018 over a wide slenderness range [1, 6]. Thus, further experimental evidence and transparent benchmarking are required to support the reliable design of multi-limb built-up CFS compression members [14–15].

To clearly position the contribution relative to prior work, Table 1 provides a concise comparison of representative studies, emphasizing the extent to which DSM and EWM have been validated for different built-up typologies and identifying the remaining gaps for hybrid multi-limb assemblies. In this context, the novelty of the present study is threefold: (1) it provides a unified experimental dataset covering four built-up configurations (CU, CC, C2U2 and C3U) and their single-limb counterparts using consistent material, fabrication, and screw layout; (2) it identifies the governing buckling-mode transition with global slenderness and links the transition to the underlying code assumptions; and (3) it delivers a head-to-head benchmark of GB 50018-2002 EWM versus AISI S100 EWM/DSM for both built-up and single-limb members, thereby clarifying accuracy, conservatism, and applicability for design engineers.

Table 1 Representative studies on built-up cold-formed steel compression members and coverage of DSM vs. EWM validation

Study (Ref.)	Member type / key variables	Design methods assessed	Key gap/relevance to present work
Selvaraj & Madhavan (2023) [1]	Built-up closed (box) CFS columns; parametric evaluation of section and member parameters	GB/AISI-based predictions (EWM/DSM depending on study scope)	Primarily focuses on closed boxes; limited evidence for hybrid C–U multi-limb sections
Nie et al. (2022) [2]	Four-channel built-up box columns under axial compression	Code-based strength checks (EWM/DSM)	Closed multi-limb only; cross-code benchmarking remains limited for open/hybrid assemblies
Gurupatham et al. (2022) [7]	Built-up open & closed channel columns with intermediate stiffeners	Design strength comparisons with stiffener effects	Highlights stiffener sensitivity; does not address CU-type multi-limb configurations
Gurupatham et al. (2025) [8]	Face-to-face unequal-angle CFS columns with stiffeners	EWM/DSM comparisons considering stiffeners	Angle built-ups with stiffeners; different symmetry and interaction mechanism than C–U multi-limb
Ananthi et al. (2024) [9]	Unsymmetrical back-to-back CFS angles under compression	Testing, modelling, and design recommendations	Provides angle-section evidence; does not cover closed CC/C2U2/C3U typologies
Wang et al. (2024) [10]	Cold-formed steel telescopic studs; screw configuration effects	Comparisons to multiple standards for connection/member strength	Informs screw-layout sensitivity; not a dataset for multi-limb built-up column typologies
Ananthi et al. (2022) [11]	Back-to-back unequal angles with intermediate stiffeners	Experiments + design strength assessment	Demonstrates interaction control by fastener spacing; configuration differs from C/U multi-limb sections
Ananthi et al. (2021) [12]	Web-stiffened battened built-up stainless steel channel columns	Nonlinear FE + proposed design equation	Reinforces need for clear critical-load definitions; present work addresses this for carbon-steel C/U assemblies
Present study	CU, CC, C2U2 and C3U built-up columns + single-limb; wide slenderness range	GB 50018-2002 EWM and AISI S100 EWM/DSM	Unified dataset and cross-code benchmarking; explicit mode-transition thresholds for design

Accordingly, this study conducts concentric axial compression tests on single-limb C- and U-sections and on four built-up configurations (CU, CC, C2U2, and C3U) fabricated from 1.0 mm-thick high-strength steel sheets with self-drilling screw connections, covering five member lengths (500–3000 mm). The specific contributions of this work are: (1) providing a consistent experimental database that enables direct comparison between single-limb and multi-limb built-up members; (2) identifying the governing buckling modes and their transition with increasing global slenderness for both open and closed configurations; (3) quantitatively assessing the prediction accuracy and conservatism of the Chinese EWM and the AISI-based EWM/DSM provisions using the same test set; and (4) evaluating the built-up coefficient to quantify the degree of structural integrity/composite action as a function of slenderness and configuration. These results provide practical guidance on the applicability of current code-based methods for CFS built-up columns.

2. Test for Axial Compression Bearing Capacity of Composite Sections

Section 2 first outlines the experimental program adopted to establish a consistent database for subsequent code evaluation and numerical modelling. The specimen matrix, fabrication details, connection layout, and test set-up are described in Sections 2.1–2.3, while Section 3 interprets the observed buckling modes and load–displacement responses.

2.1. Specimen Design

The experimental program considered three primary parameters: cross-section configuration, member length, and the associated global slenderness ratio. Six section types were examined, including single-limb C-and U-sections and four screw-assembled built-up sections (CU, CC, C2U2, and C3U) fabricated by combining C- and U-shaped elements, as illustrated in Fig. 1.

All members were fabricated from galvanized high-strength cold-formed steel with a nominal yield strength of 550 MPa and connected using ST4.8 self-drilling, self-tapping screws; the screw layout followed relevant Chinese and Australian provisions (Table 2). To determine the intermediate screw spacing, the provisions for built-up compression members in AISI S100-2007 were adopted. Specifically, the spacing a between adjacent screws was selected such that the slenderness of an individual limb segment between fasteners (a/r_i, where r_i is the minimum radius of gyration of a single-limb component) does not exceed one-half of the overall member slenderness ratio of the built-up column, i.e.

$$\frac{a}{r_i} \le 0.5\left(\frac{KL}{r}\right)_o \tag{1}$$

Here, K is the effective length factor (K =1.0 for the pin-ended tests), L is the member length, and r is the radius of gyration of the built-up section. In addition, the end fastener arrangement and edge distances were checked to satisfy the corresponding screw detailing requirements. The resulting screw layouts (including a and end margin) are summarized in Table 3.

Cross-sectional properties (area, centroid coordinates, and second moments of area) are summarized in Table 2. Five member lengths were adopted: 500 mm, 1000 mm, 1500 mm, 2000 mm, and 3000 mm. Tests were performed under displacement control (0.2 mm/min) with double knife-edge hinges at both ends; the loading rig is shown in Fig. 2, and a vertical displacement transducer was installed beneath the hydraulic jack. As an example of the specimen identification scheme, "5C-1" denotes a 500 mm-long C-section specimen, replicate no. 1.

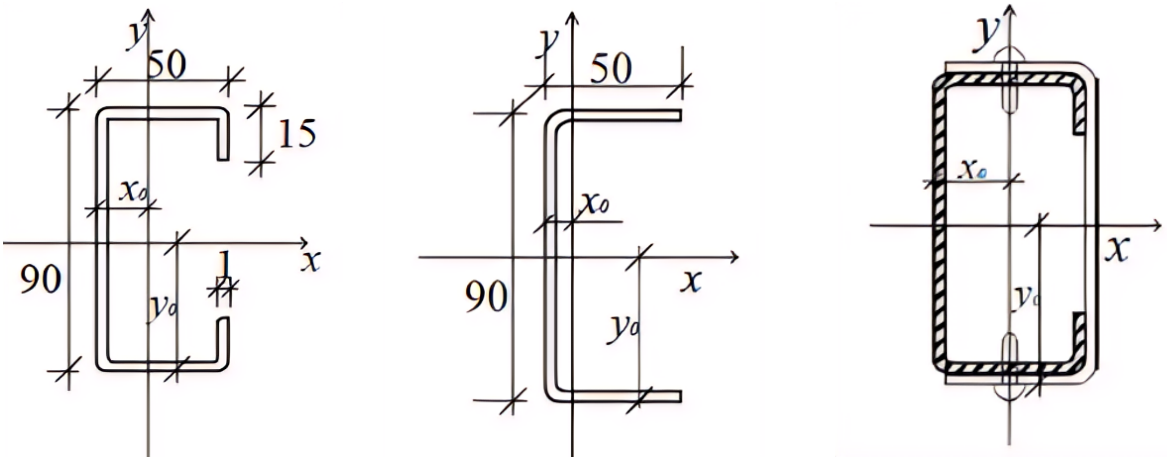

(a) C-shaped section (b) CU-shaped section (c) C2U2-shaped section

Fig. 1 Member section and arrangement of the strain gauge

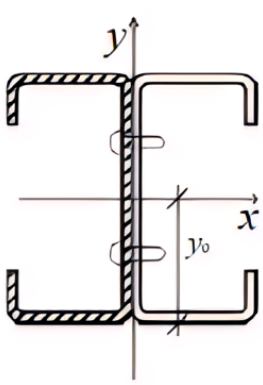

(d) U-shaped section

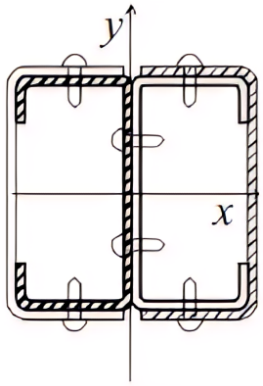

(e) CC-shaped section

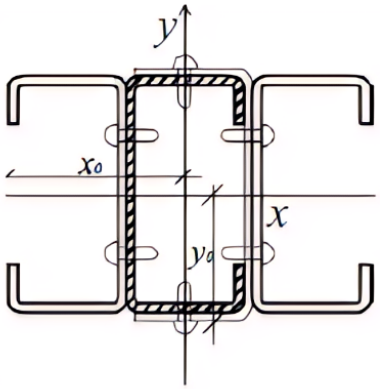

(f) C3U-shaped section

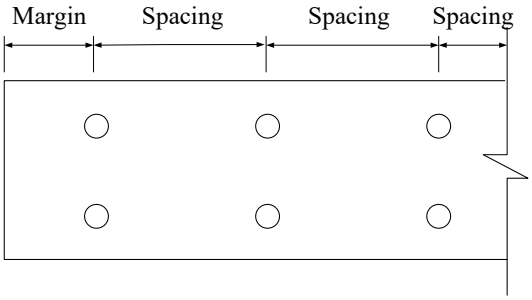

(g) Pitch Schematic Diagram

Fig. 1 Member section and arrangement of the strain gauge (continued)

Table 2 The Dimensions of basic specimens

Cross-section	Cross-sectional area A (mm^2)	Centroid x_0 (cm)	Centroid y_0 (cm)	Moment of inertia I_x (cm^4)	Moment of inertia I_y (cm^4)
U	188	1.35	4.60	26.57	4.91
C	216	1.81	4.50	28.96	7.92
CU	404	2.37	4.60	55.73	16.66
CC	432	5.00	4.50	57.92	29.90
C2U2	836	5.10	4.60	111.46	93.47
C3U	864	7.64	4.60	113.66	112.03

Table 3 Spacing between screws

Cross-section		500mm	1000mm	1500mm	2000mm	3000mm
CU	Margin	100	100	150	100	150
	Spacing	150	200	200	300	300
CC	Margin	100	100	150	100	150
	Spacing	150	200	200	300	300
C2U2	Margin	50	100	150	100	150
	Spacing	100	200	200	300	300
C3U	Margin	50	100	150	100	150
	Spacing	100	200	200	300	300

2.2. Loading and Testing System

Tests were carried out on a YAW-10000F microcomputer-controlled servo-hydraulic compression machine with a rated axial capacity of 1000t. To simulate pin-ended boundary conditions under axial compression, double knife-edge hinges were installed at both specimen ends (test rig shown in Fig. 2). The clamping plates connecting the hinges to the specimens were fastened with ST4.8 self-drilling screws; after end leveling and clamping, the screws were tightened using a hand drill. Loading was applied under displacement control at 0.2 mm/min to capture the ultimate capacity and failure mode.

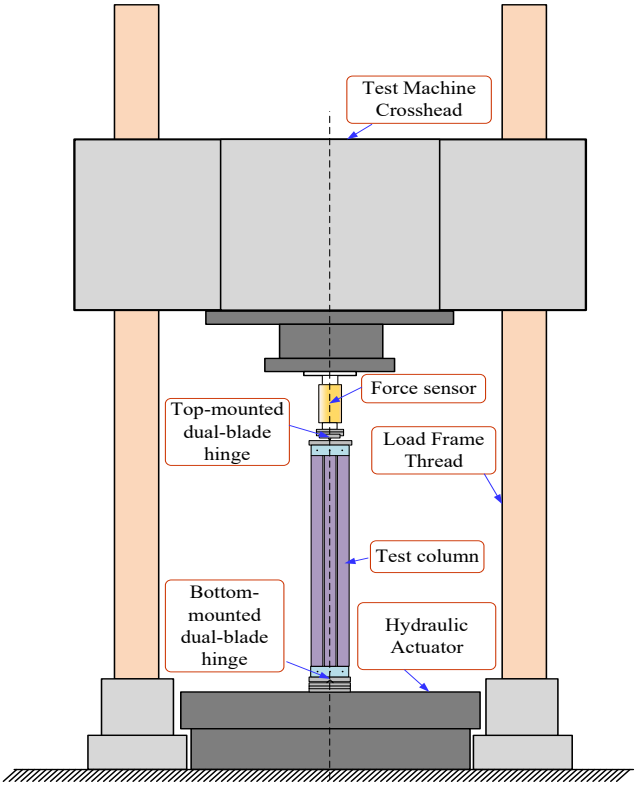

(a) Loading Schematic Diagram

(b) Top Double-Knife Edge Hinge

(c) Bottom Double-Knife Edge Hinge

Fig. 2 Pictures of the loading system

Before testing, alignment was verified with a level to minimize initial eccentricity and ensure concentric loading. To quantify and control the initial loading eccentricity, a seating (preload) stage was performed prior to the formal test. A small seating load (about 2–5% of the expected ultimate load) was applied to allow the hinges and clamping system to self-align. During this stage, the paired horizontal displacement transducers (S1–S6) arranged in symmetric pairs at 1/4H, 1/2H, and 3/4H (or S1–S2 at mid-height for the 500 mm columns) were monitored. The specimen position was fine-tuned by end leveling and centering until each symmetric pair showed nearly identical lateral readings.

An initial eccentricity indicator $e_0$was then evaluated from the mid-height lateral displacement $u_0$under the seating load and normalized by the specimen length H as in the present test series, the columns were only accepted for formal loading when this normalized eccentricity satisfied $e_0/H \leq 1.0 \times 10^{-3}$, and the difference between the readings of each symmetric transducer pair was less than 0.1 mm. For all 60 specimens, the measured values of e_0/Hmet this criterion, indicating that the initial eccentricity level was small compared with the member length, with mid-height offsets on the order of sub-millimetres

to a few millimetres depending on the column length. The vertical load was recorded by a 500 kN load cell. Each test was continued into the post-peak regime and terminated when the load had dropped to approximately 30% of its peak value, thereby obtaining the complete load–axial displacement curve.

Initial geometric imperfections may influence the buckling response of cold-formed thin-walled members. In this experimental program, full-field measurements of the initial geometric imperfections (including local plate waviness and global member out-of-straightness) were not carried out prior to loading (e.g., by laser scanning). The initial eccentricity indicator adopted in this study, evaluated from the mid-height lateral displacement under the seating load, should therefore be interpreted as a global and indirect measure that combines all sources of out-of-straightness, including specimen geometric imperfections and residual test-set-up misalignment, rather than as a "pure" geometric imperfection amplitude of the member. Although specimen dimensions were checked during fabrication/assembly, the end surfaces were levelled, and the loading alignment was verified before testing to minimize unintended eccentricity. This approach cannot decouple the respective contributions of fabrication imperfections and loading eccentricity; instead, it was used as a practical criterion to keep the combined imperfection within a narrow band across specimens.

Consequently, the absolute values of the ultimate capacities and the exact slenderness thresholds for transitions between local, distortional, global, and interactive buckling modes should be interpreted in the context of typical combined imperfection levels rather than as responses to a uniquely defined imperfection shape. For full-field imperfection measurement and modelling strategies for built-up thin-walled members, see, for example, Jiang and Zhao [16] and Ma et al. [17].

For all specimens except those with a length of 500 mm, two vertical displacement transducers (UH1, UH2) and six horizontal displacement transducers (S1–S6) were installed; the six horizontal gauges were arranged in pairs at heights of 1/4, 1/2, and 3/4 of the specimen. For the 500 mm columns, two vertical (UH1, UH2) and two horizontal (S1, S2) displacement transducers were symmetrically placed at mid-height. The instrumentation layout and labeling are shown in Fig. 3.

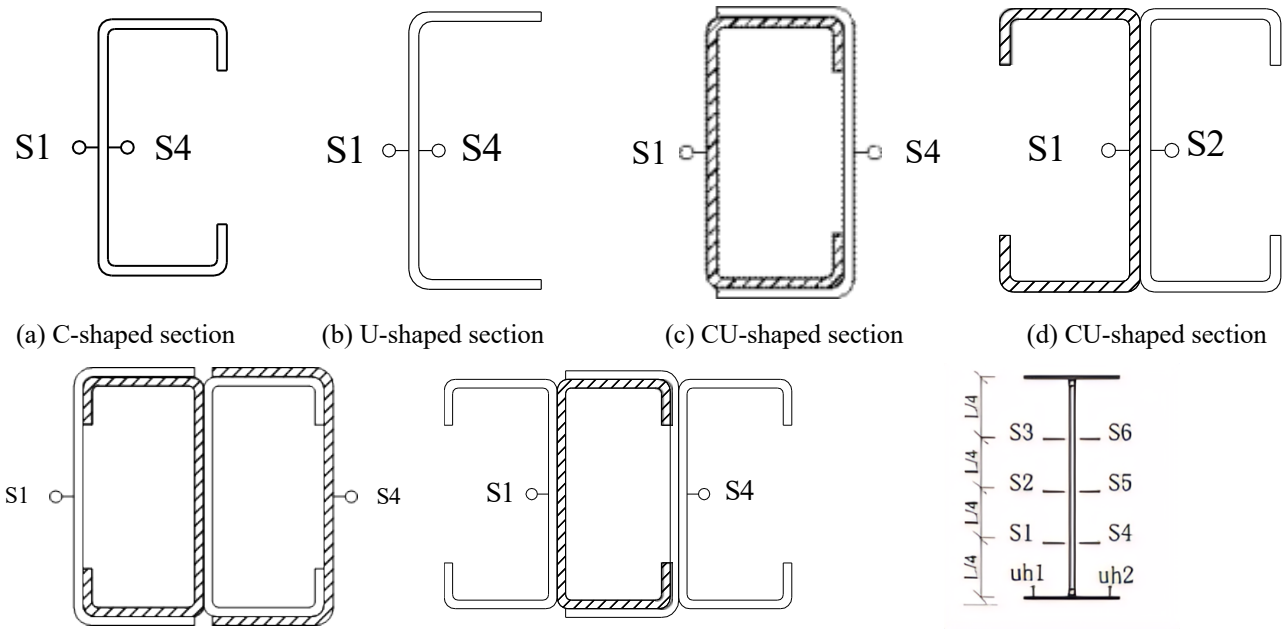

(a) C-shaped section (b) U-shaped section (c) CU-shaped section (d) CU-shaped section

(e) C2U2-shaped section (f) C3U-shaped section (g) Vertical Displacement Transducer

Fig. 3 Displacement Transducer Layout

To capture the stress evolution of different cross-sections under axial compression, strain gauges were mounted at mid-height (1/2H) for the 500 mm specimens, and at 1/4H, 1/2H, and 3/4H for the longer specimens. The gauge locations for each section type are shown in Fig. 4.

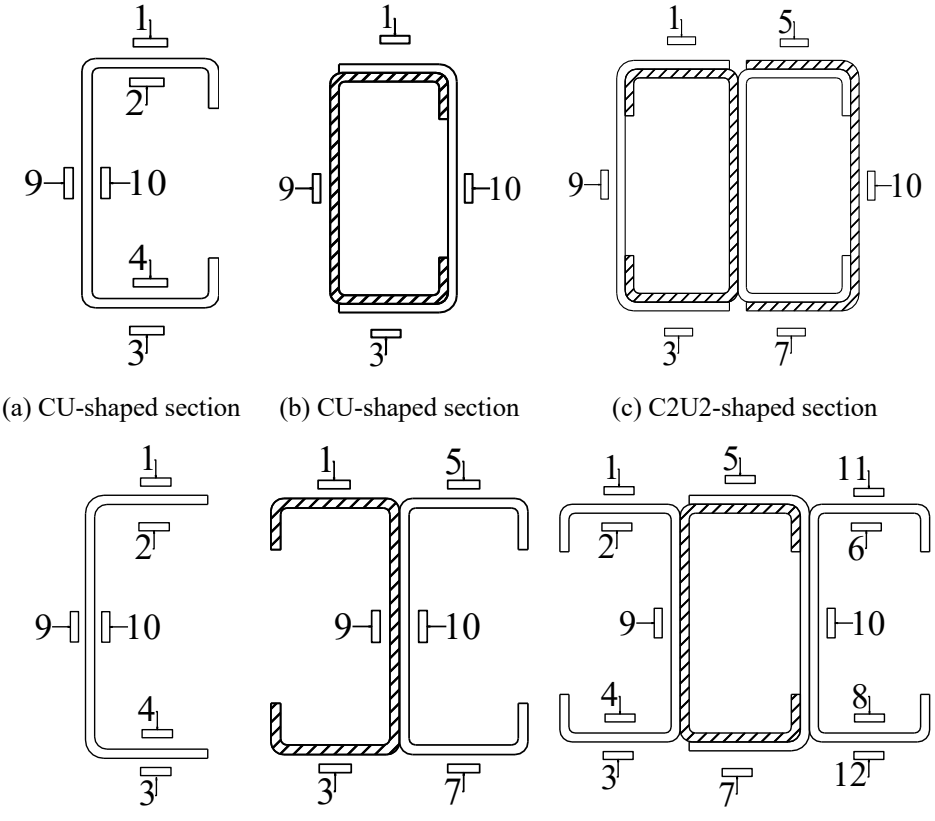

(a) CU-shaped section (b) CU-shaped section (c) C2U2-shaped section

(d) U-shaped section (e) CC-shaped section (f) C3U-shaped section

Fig. 4 Arrangement of the strain gauge

2.3. Material Property Tests

Specimens were fabricated from a one mm-thick high-strength cold-formed steel sheet. Material coupons were prepared in accordance with Metallic Materials—Tensile Testing—Part 1: Method of Test at Room Temperature (GB/T 228.1-2010), with dimensions shown in Fig. 5(a). The sampling locations and specimen extraction procedure followed the requirements of GB/T 2975-2018 (Steel and steel products—Location and preparation of samples and test pieces for mechanical testing) and ISO 377:2017. Specifically, coupons were taken from the flat portions of the sheet/sections (web and flange) along the longitudinal (rolling) direction and away from the corner radii to avoid the influence of localized cold-working in the corner regions [18-20]. Coupons were extracted from: (i) flat sheet not subjected to cold forming, (ii) the web and flange of the U-section, and (iii) the flange of the C-section. Six standard coupons were cut along the longitudinal (rolling) direction. Tensile tests were performed on a microcomputer-controlled electronic tensile testing machine, as shown in Fig. 5(b).

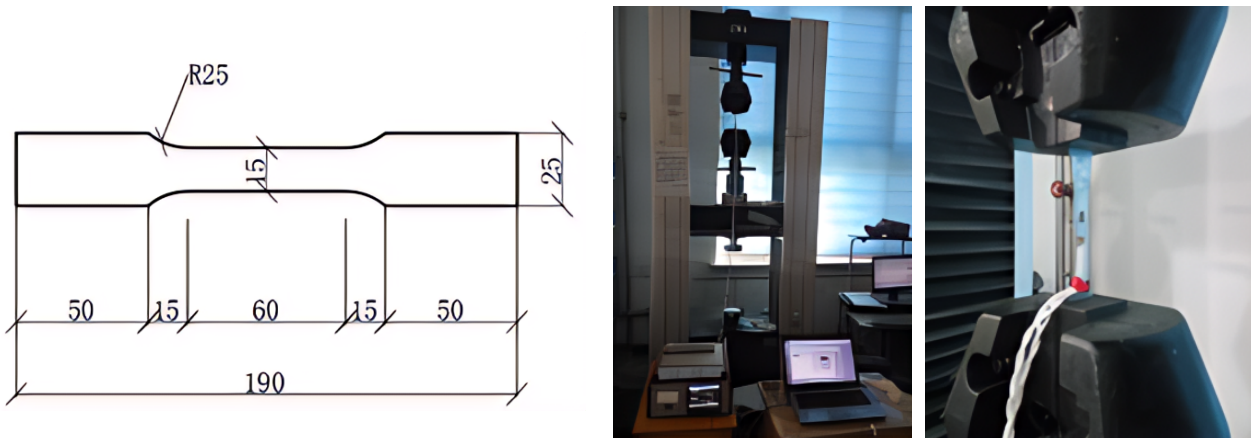

(a) Dimensions of the material specimen (b) Photograph of the tensile test on the material specimen

Fig. 5 Picture of the material test

Cold-formed thin-walled steel typically exhibits no distinct yield plateau; therefore, the yield stress was determined using the 0.2% proof stress method. The corresponding stress–strain curves are presented in Fig. 6, and the individual coupon results are summarized in Table 3. For the seven coupons tested in this study, the mean yield stress was 505.9 MPa with a standard deviation of 55.3 MPa, and the mean elastic modulus was 195.5 GPa with a standard deviation of 10.3 GPa. The location-dependent scatter reflects the combined effects of base material variability and strain hardening induced by the cold-forming process.

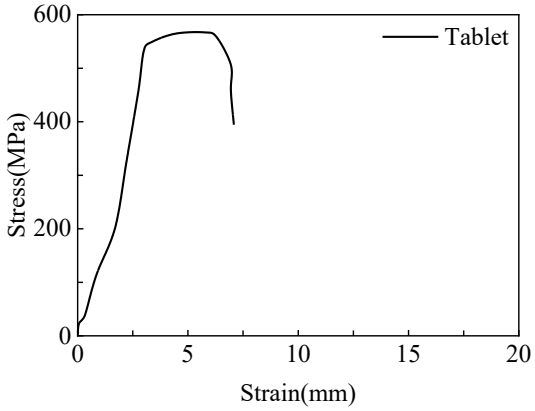

(a) Stress–strain curve of the flat sheet

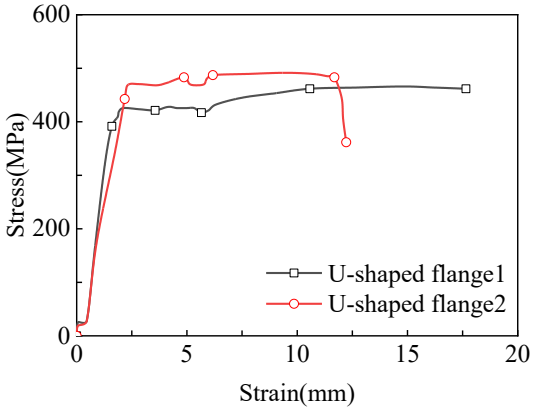

(b) Stress–strain curve of the U-section flange

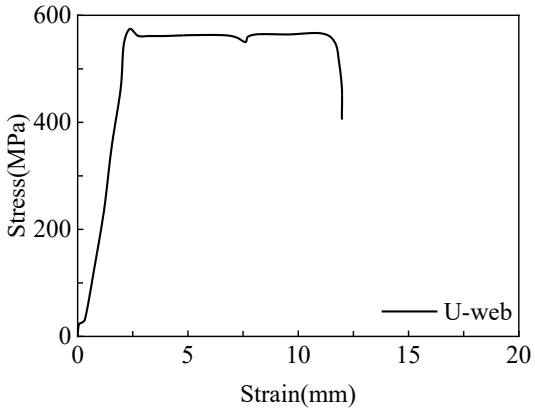

(c) Stress–strain curve of the U-section web

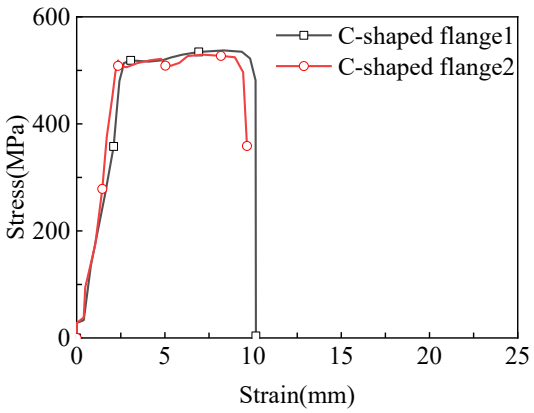

(d) Stress–strain curve of the C-section flange

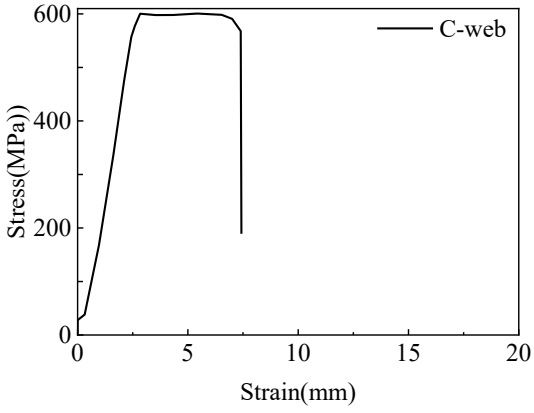

(e) Stress–strain curve of the C-section web

Fig. 6 Picture of the material test

As shown in Table 4, the web regions of the C-and U-sections generally exhibit higher yield and ultimate strengths than the flange regions, which is attributed to non-uniform plastic straining during roll-forming. This cold-working effect increases strength but can reduce ductility; therefore, location-specific coupon data were used when interpreting the strain-gauge measurements and when selecting material parameters for subsequent analytical comparisons.

Table 4 Material test results

Specimen name		Position	Yield stress σ_y (MPa)	Limit stress σ_u (MPa)	Elongation %	Modulus of elasticity E/GPa
3		Tablet	488.67	563.33	10.4%	203.01
T25	Type C	C-flange	512.67	532.00	11.19%	201.40
T26		C-flange	506.67	525.33	11.36%	198.60
T24		C-web	582.67	601.33	7.81%	203.80
T21	Type U	U-flange	420.67	462.67	24.44%	179.00
T23		U-flange	466.67	491.33	13.39%	182.50
T22		U-web	563.33	570.67	13.84%	200.30

3. Experimental Results and Discussion

Section 3 presents the experimental observations and key trends from the axial compression tests. Section 3.1 describes the typical failure modes and load–displacement responses for each cross-section, while Section 3.2 synthesizes the test results in terms of ultimate capacities, stiffness characteristics, and governing buckling modes.

3.1 Experimental Observations

The six cross-sectional configurations tested can be broadly classified into three categories: open, closed, and semi-closed sections. For shorter specimens, the buckling of open and semi-closed sections was governed by distortional buckling. As the slenderness ratio increased, the dominant buckling mode transitioned from distortional to local buckling. When the specimen length reached 3 m, all sections failed predominantly by global buckling. Given the distinct failure patterns associated with different section types, the observed failure modes for the six configurations are summarized as follows: For quantitative context, the slenderness ratio (λ) and the measured ultimate load (P_u) of each specimen are reported in Table 4; representative ranges are also cited below when describing each failure mode.

All specimens were tested under nominally pin-ended boundary conditions (double knife-edge hinges), which allow end rotation while restraining translation. Therefore, for members with relatively large global slenderness, the first-mode flexural (global) buckling response is expected and was observed. For stocky members, local plate buckling and/or distortional buckling initiated in the slenderest plate elements under compressive membrane stresses, manifesting as out-of-plane buckling waves. In addition to the photographic evidence, the strain gauges (Fig. 4) were used to corroborate the onset and location of buckling through the abrupt change in strain distribution among adjacent gauges.

Initial geometric imperfections were minimized through the alignment procedures described in Section 2.2; nevertheless, the observed scatter in open single-limb sections indicates a higher sensitivity to combined geometric imperfections and loading eccentricity compared with closed built-up sections. Because global out-of-straightness and local plate waviness were not measured explicitly, the present results should be regarded as representative of typical as-built imperfection levels under standard alignment tolerances, rather than as a systematic parametric study on imperfection sensitivity. In particular, the occurrence of interactive local–distortional–global buckling in some medium-length specimens reflects the combined effect of the structural characteristics and the unmeasured imperfection fields; future work incorporating full-field imperfection measurements would be required to fully disentangle these effects.

In this study, the term “ripples” refers to local plate buckling half-waves that develop in slender flat elements (webs or flanges) under axial compression. Their appearance indicates the onset of local buckling when the compressive stress in a plate element approaches its elastic critical plate-buckling resistance; after buckling, stresses redistribute within the element, and

the effective-width concept becomes relevant (see Section 4.2). The subsequent amplification of these buckle waves reduces stiffness and may trigger interaction with distortional buckling (flange rotation about the web–flange junction) and/or global flexural buckling, depending on the member slenderness ratio.

U-Section: During loading, as the axial force increased, local plate buckling waves (rippling) initiated in the flanges and webs, indicating the onset of local buckling and the beginning of stiffness degradation. As shown in Fig. 7, after a relatively long loading duration, the flange of specimen 5U exhibited *V*-shaped distortional buckling, which triggered the failure of the entire specimen and caused a sudden drop in load-carrying capacity. For specimens 10U and 15U, numerous ripples formed in the flanges and webs, resulting in local buckling and a gradual decrease in load capacity.

Observations from specimens 20U and 30U indicate that once global buckling occurred, the lateral displacement increased significantly and the load capacity decreased. With continued loading, a *V*-shaped stiffening fold—indicative of distortional buckling—was observed in the flange at a localized region of the specimen. Quantitatively, the short U-section specimens 5U (λ=31.02) reached P_u=12.34-12.50 kN and failed by distortional buckling; intermediate specimens 10U and 15U (λ=62.04 and 93.06) reached P_u =9.10-9.41 kN and 7.10-7.87 kN and exhibited local buckling; the slender specimens 20U and 30U (λ=124.08 and 186.13) reached P_u =5.71-7.40 kN and approximately 5.25 kN and failed by global buckling.

(a) Distortional buckling (b) Local buckling (c) Global buckling

Fig. 7 Buckling modes of U-section specimens

As shown in Fig. 8, when the load increases to a certain level, the flanges of the specimens exhibit inward contraction or outward expansion, and slight buckling waves appear on the webs. With further loading, the specimens eventually fail due to excessive distortion buckling deformation, resulting in a complete loss of load-bearing capacity. When the slenderness ratio exceeds 110, the buckling mode shifts from distortion buckling to global buckling. For specimens 10CC, 15CC, and 20CC, after the load-bearing capacity decreases and loading continues, distortion buckling occurs again at other locations, forming sharp tips. At this stage, the load-bearing capacity decreases further, ultimately reducing to about 60% of the ultimate load. In terms of measured capacities, the open C-sections (5C to 20C, λ=25.99-103.96) exhibited distortional buckling with P_u=16.82-36.42 kN, while 30C (λ=155.94) showed global buckling with P_u =10.03-10.18 kN; for the closed CC-sections, distortional buckling governed for 5CC to 20CC (λ=18.92-75.67) with P_u =48.14-72.83 kN, whereas 30CC (λ=113.50) failed by global buckling with P_u =34.58-35.95 kN.

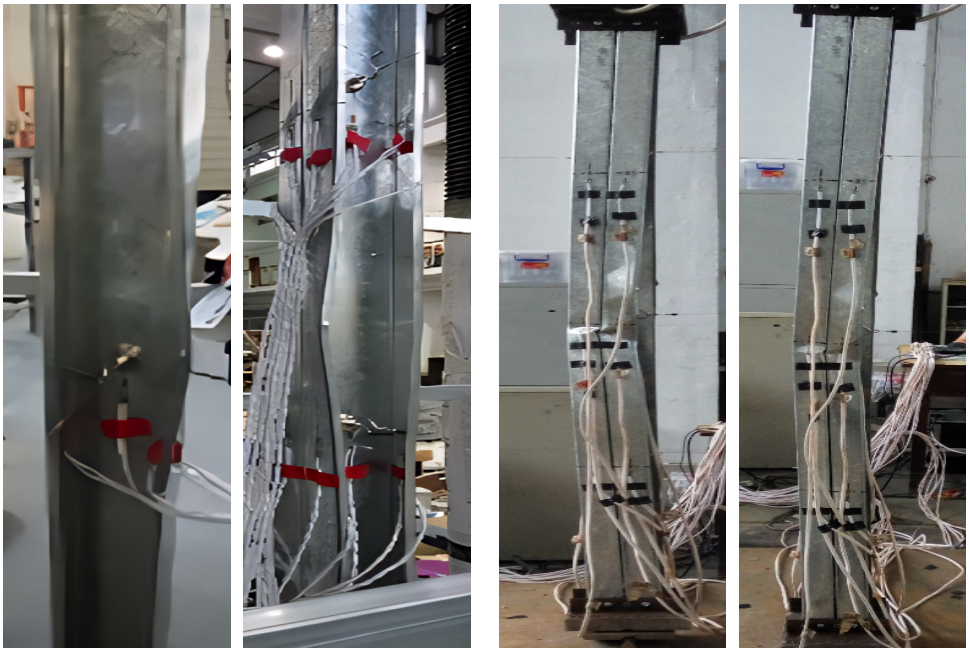

(a) Distortional buckling (b) Global buckling

Fig. 8 Buckling modes of C- and CC-section specimens

As shown in Fig. 9, with the increase of load, local plate buckling waves initiated on the flanges of the external U-shaped section and gradually developed on the webs of both the C-shaped and U-shaped sections. When the load reaches a certain level, closed sections with a slenderness ratio less than 70 experience significant bending deformation and local buckling, causing the load-bearing capacity to drop by about 50%. However, for specimens with a slenderness ratio greater than 70, global buckling occurs instead, resulting in increased displacement but without a significant reduction in load-bearing capacity. After global buckling, local buckling will continue to develop at a specific location, resulting in a further decrease in the load-bearing capacity to approximately 50% of the ultimate load. For the CU specimens, local buckling was observed for 5CU and 10CU (λ=24.62 and 49.24, P_u=54.16-65.42 kN), whereas global buckling occurred for 15CU to 30CU (λ=73.83-147.73, P_u =25.32-50.15 kN). For the C2U2 specimens, local buckling governed up to 20C2U2 (λ=14.70-58.80, P_u =107.24-133.55 kN), while global buckling occurred for 30C2U2 (λ=88.20, P_u =76.22-80.08 kN).

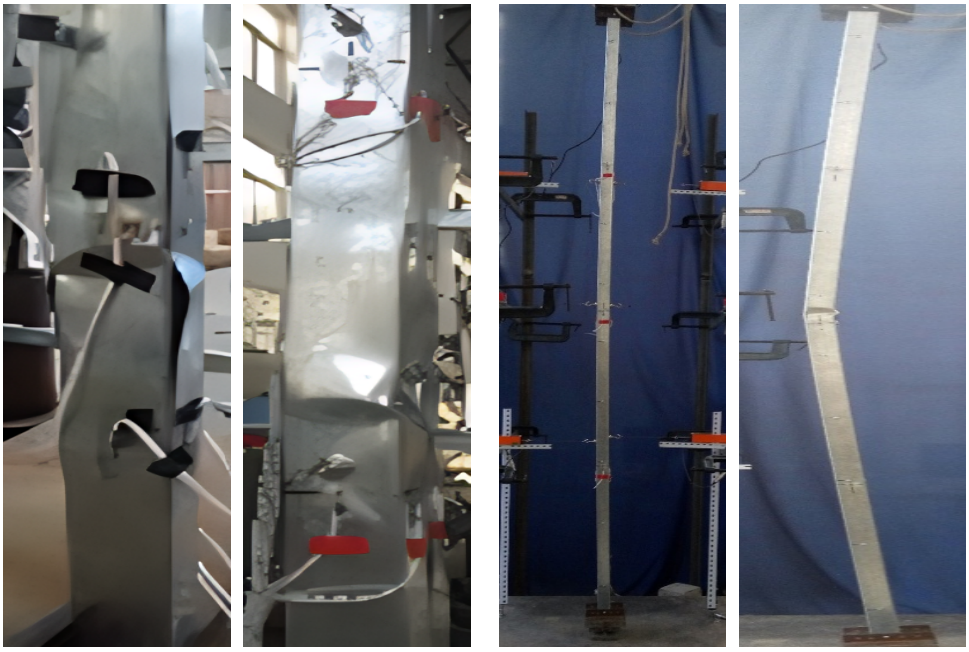

(a) Local buckling (b) Global buckling

Fig. 9 Buckling modes of CU- and C2U2-section specimens

As shown in Fig. 10, during the loading process, the C-shaped flanges on both sides of the specimen contract inward, and local plate buckling waves develop on the U-shaped flanges. With further load increase, the C3U specimen with a slenderness ratio of 30 exhibits overall buckling while simultaneously undergoing distortion and local deformation. However, for medium-length columns, the buckling mode is mainly governed by the combined effect of distortional buckling and local buckling. For the short-column specimen (5C3U), only the flanges on both sides at the bottom contract inward, showing distortional buckling, while no significant phenomenon is observed in the middle-closed section. For the C3U built-up section, distortional buckling dominated 5C3U (λ=13.51, P_u =133.16-133.32 kN), combined distortional-local buckling occurred for 10C3U to 20C3U (λ=27.01-54.02, P_u =99.06-137.79 kN), and the slenderest 30C3U (λ=81.04, P_u =89.03-95.38 kN) exhibited interactive global-distortional-local buckling.

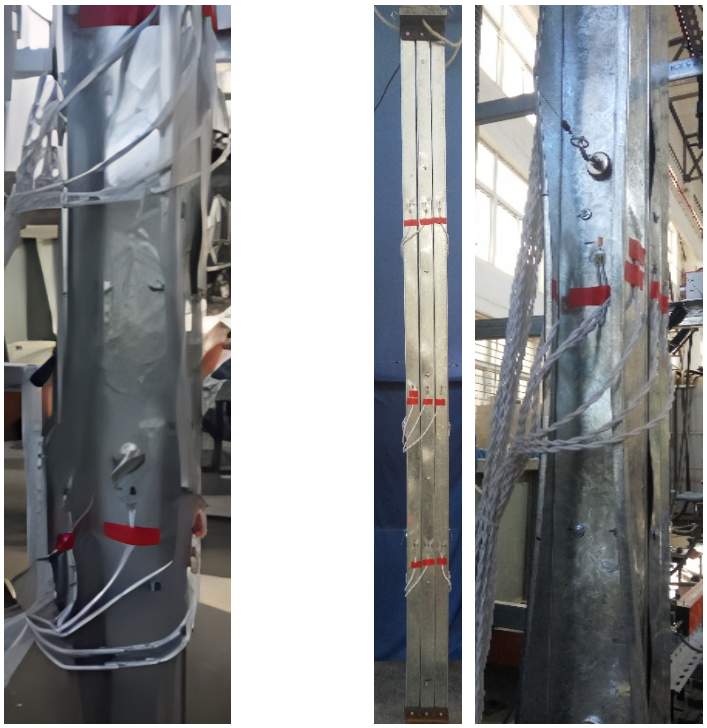

(a) Distortional + local buckling (b) Global + distortional + local buckling

Fig. 10 Buckling modes of C3U-section specimens

The vertical displacement-load relationships for specimens with different cross-sections are shown in Fig. 11. For local buckling and distortional buckling, the specimens exhibit brittle failure, with the load-carrying capacity dropping to 60% of the ultimate capacity. In contrast, for overall buckling, the vertical displacement-load–load curve shows a gradual descending trend.

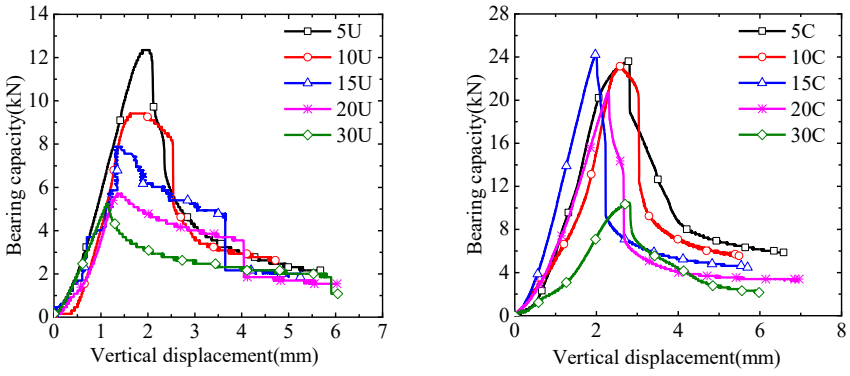

(a) U-section (b) C-section

Fig. 11 Curves of vertical displacement vs load of shape specimens

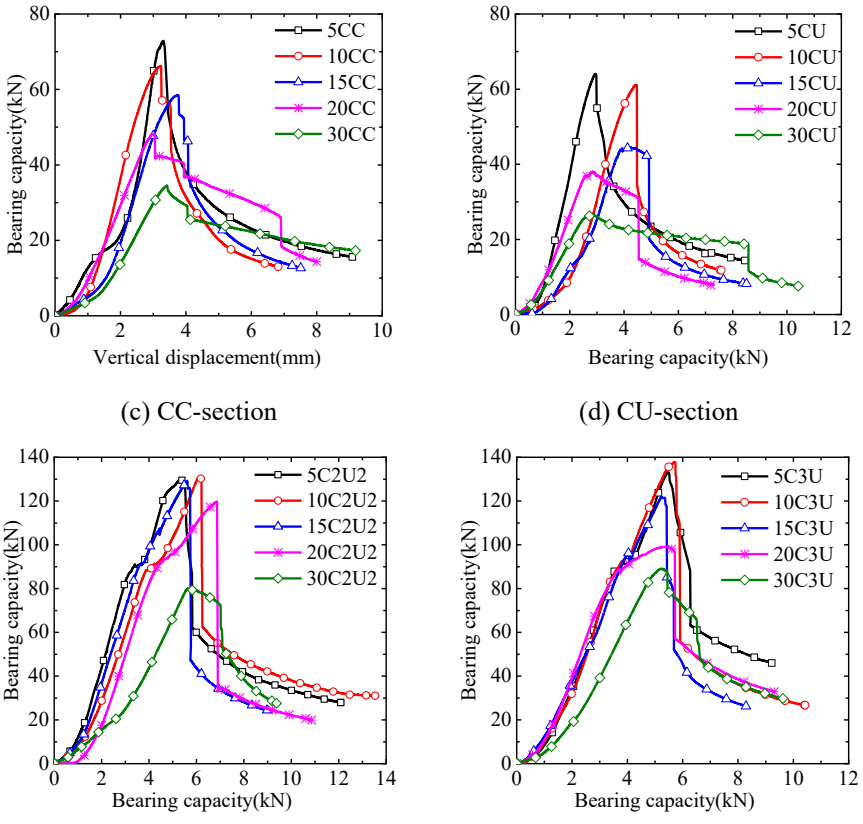

(c) CC-section (d) CU-section

(e) C2U2-section (f) C3U-section

Fig. 11 Curves of vertical displacement vs load of shape specimens (continued)

3.2 Results and Discussion

The vertical load–axial displacement (P–δ) curves for specimens with different cross-sections are shown in Fig. 11. All specimens exhibit an approximately linear response at the early loading stage; as the load approaches the peak capacity, the axial stiffness degrades due to the onset of plate buckling (local/distortional) and/or growth of lateral deflection. Specimens governed by local or distortional buckling display a relatively abrupt post-peak strength drop, whereas specimens governed by global buckling show a more gradual descending branch with larger post-peak deformation capacity.

To facilitate comparison of curve features, the initial axial stiffness K_0 is evaluated as the secant stiffness between $0.1P_u$ and $0.4P_u$, where δ_x denotes the axial displacement corresponding to xP_u. The deformation capacity is characterized by δ_u, defined as the displacement at which the load first drops to $0.8P_u$ on the post-peak branch. Accordingly, the displacement ductility index is defined as $\mu = \delta_u/\delta_{0.75}$, with $\delta_{0.75}$ taken at 0.75 P_u on the ascending branch as a practical reference point for thin-walled members without a distinct yield plateau.

Overall, K_0 decreases with increasing member length (and thus increasing slenderness ratio λ). At comparable λ, built-up closed sections (C2U2 and C3U) generally present higher stiffness and better post-peak deformation capacity than single-limb open sections, owing to improved torsional rigidity and mutual restraint among the connected limbs.

The measured load-carrying capacities and failure modes of all specimens are summarized in Tables 4 and 5. In these tables, D represents distortional buckling, L represents local buckling, and G represents global buckling, while D+L indicates that distortional and local buckling occurred simultaneously. The member slenderness ratio is defined as $\lambda = KL/r_{\min}$, where L is the member length, K is the effective length factor (K=1.0 for the pin-ended conditions provided by the double knife-edge hinges), and $r_{\min} = \sqrt{\frac{I_{\min}}{A}}$ is the minimum radius of gyration of the gross cross-section.

Table 5 Comparison of experimental values

Name	Slenderness ratio	P_u	Mode	P-Ave	Name	Slenderness ratio	P_u	Mode	P-Ave
5U-1	31.02	12.34	D	12.42	5C-1	25.99	28.08	D	25.85
5U-2		12.50	D		5C-2		23.61	D	
10U-1	62.04	9.10	L	9.62	10C-1	51.98	36.42	D	24.07
10U-2		9.41	L		10C-2		23.13	D	
15U-1	93.06	7.87	L	7.48	15C-1	77.97	20.99	D	22.61
15U-2		7.10	L		15C-2		24.23	D	
20U-1	124.08	7.40	G	6.55	20C-1	103.96	16.82	D	18.75
20U-2		5.71	G		20C-2		20.68	D	
30U-1	186.13	5.246	G	5.25	30C-1	155.94	10.184	G	10.11
30U-2		5.246	G		30C-2		10.030	G	
5CU-1	24.62	54.16	L	59.10	5CC-1	18.92	72.83	D	68.74
5CU-2		64.04	L		5CC-2		64.65	D	
10CU-1	49.24	63.88	L	61.49	10CC-1	37.83	66.20	D	66.97
10CU-2		61.04	L		10CC-2		67.74	D	
15CU-1	73.83	50.15	G	47.29	15CC-1	56.75	58.48	D	58.48
15CU-2		44.44	G		15CC-2		58.48	D	
20CU-1	98.49	44.75	G	41.43	20CC-1	75.67	56.32	D	52.23
20CU-2		38.11	G		20CC-2		48.14	D	
30CU-1	147.73	26.385	G	26.93	30CC-1	113.50	35.953	G	35.27
30CU-2		27.465	G		30CC-2		34.595	G	
5C2U2-1	14.70	107.24	L	130.08	5C3U-1	13.51	133.16	D	133.24
5C2U2-2		130.08	L		5C3U-2		133.32	D	
10C2U2-1	29.04	130.80	L	132.18	10C3U-1	27.01	137.79	D+L	138.64
10C2U2-2		133.55	L		10C3U-2		118.04	D+L	
15C2U2-1	44.10	113.87	L	121.51	15C3U-1	40.52	116.50	D+L	119.28
15C2U2-2		129.15	L		15C3U-2		122.05	D+L	
20C2U2-1	58.80	113.38	L	116.56	20C3U-1	54.02	118.81	D+L	108.94
20C2U2-2		119.74	L		20C3U-2		99.06	D+L	
30C2U2-1	88.20	76.224	G	78.15	30C3U-1	81.04	95.375	G+D+L	92.20
30C2U2-2		80.082	G		30C3U-2		89.031	G+D+L	

To quantify repeatability, two nominally identical specimens were tested for each cross-section type and member length. The scatter of ultimate capacity is evaluated using the coefficient of variation (COV=s/mean) and the relative difference ΔP_u = (max−min)/mean. As summarized in Table 6, the built-up sections exhibit a lower average scatter (mean COV=6.24%) than the single-limb sections (mean COV=9.83%), indicating that the multi-limb assembly provides enhanced restraint and reduced imperfection sensitivity. *A* larger scatter is observed for open single-limb sections, where local/distortional deformations are more sensitive to small geometric imperfections.

Table 6 Repeatability statistics of ultimate capacities in replicate tests

Section type	No. of replicate pairs	Mean COV of P_u (%)	Max COV (%)	Max ΔP_u(%)
Built-up (all)	20	6.24	13.61	19.25
Single-limb (all)	10	9.83	31.56	44.63
U	5	5.76	18.23	25.78
C	5	13.91	31.56	44.63
CU	5	7.55	11.82	16.72
CC	5	4.77	11.07	15.66
C2U2	5	6.26	13.61	19.25
C3U	5	6.4	12.82	18.13

The relationship curves between the slenderness ratio and the ultimate load-bearing capacity for each cross-section specimen are shown in Fig. 12, where the ultimate load-bearing capacity in the curves is taken as the average value. Test results indicate that when the slenderness ratio is less than 80, the ultimate load-bearing capacities of the different cross-sections under the same slenderness ratio are ranked as follows: C2U2 > C3U > CC > CU > C > U. When the slenderness ratio is greater than 80, the ranking changes to: C3U > C2U2 > CU > CC > C> U. This is because as the slenderness ratio increases, the buckling mode of the C2U2 section shifts from local buckling control to global buckling control, and the buckling mode of the CC section changes from distortional buckling control to global buckling control. The global buckling load-bearing capacity of each specimen's cross-section is approximately half of the ultimate load-bearing capacity of the corresponding short column.

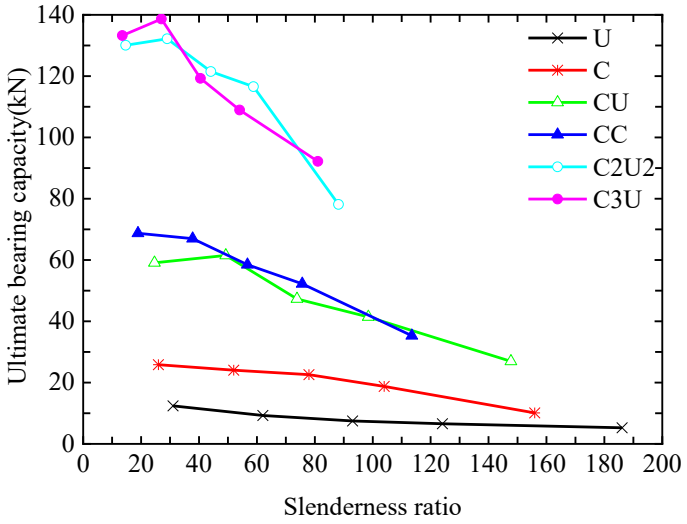

Fig. 12 Load vs slenderness ratio curve of section

The flanging of single-limb sections not only increases the slenderness ratio of the section but also enhances the restraint of the flanges. Therefore, for C-shaped sections with a slenderness ratio less than 110, the buckling is primarily governed by distortional buckling. When the length reaches 3000 mm, the slenderness ratio exceeds 150, and the section behavior is dominated by global buckling.

The buckling behavior of closed sections differs from that of open sections. In closed sections, the two single-limb components are connected by screws, providing mutual restraint and increasing the flange restraint, which prevents the occurrence of distortional buckling. For closed sections, the buckling mode at the ultimate load is governed by local buckling when the slenderness ratio is less than 70, and by global buckling when the slenderness ratio exceeds 70.

4. Code-Based Calculation Methods

Currently, the calculation of the axial load capacity of cold-formed thin-walled steel members mainly involves two methods: the Effective Width Method (EWM) and the Direct Strength Method (DSM). The Effective Width Method is based on the concept that local buckling of the plate elements causes a redistribution of stresses on the plate surface. As a result, a portion of the cross-section effectively becomes inactive, and the cross-sectional area is reduced to account for the post-buckling strength. The method assumes that post-buckling stresses are represented as a uniform distribution over an effective width across the plate element. Using extensive experimental data that considered initial imperfections and element stiffening, Winter derived the following effective-width formula:

$$b_e = 0.95t\sqrt{\frac{kE}{f_y}}\left(1-0.208\frac{b}{t}\sqrt{\frac{kE}{f_y}}\right) \tag{2}$$

In Winter's original effective-width formulation, the reduction factor is expressed as a function of the compressive stress in the plate element. In current design provisions (e.g., AISI S100-2007), the effective width is commonly calculated using the reduced plate slenderness $\lambda = \sqrt{F_y/f_{cr}}$ where F_y is the specified yield stress (taken from the coupon tests) and f_{cr} is the elastic plate buckling stress. Therefore, f_y was not estimated from the member test results (e.g., σ_{max}), and the code-based calculations reported in this study were performed strictly following the specification.

For readers' convenience, Fig. 13 shows the input–output workflow of the three design paths used in this study. Path 1 evaluates axial capacity using the Chinese code GB 50018-2002 (EWM) from gross dimensions and material properties to effective section properties and member strength. Path 2 follows the AISI S100-2007 EWM procedure, computing reduced plate slenderness, effective widths and effective section moduli before applying the column strength curves. Path 3 adopts the AISI S100-2007 DSM, where elastic local/distortional/global buckling loads (P_{cr}) from eigen-buckling analysis are combined with nominal yield resistance. This flowchart highlights the differences and common steps among the three routes.

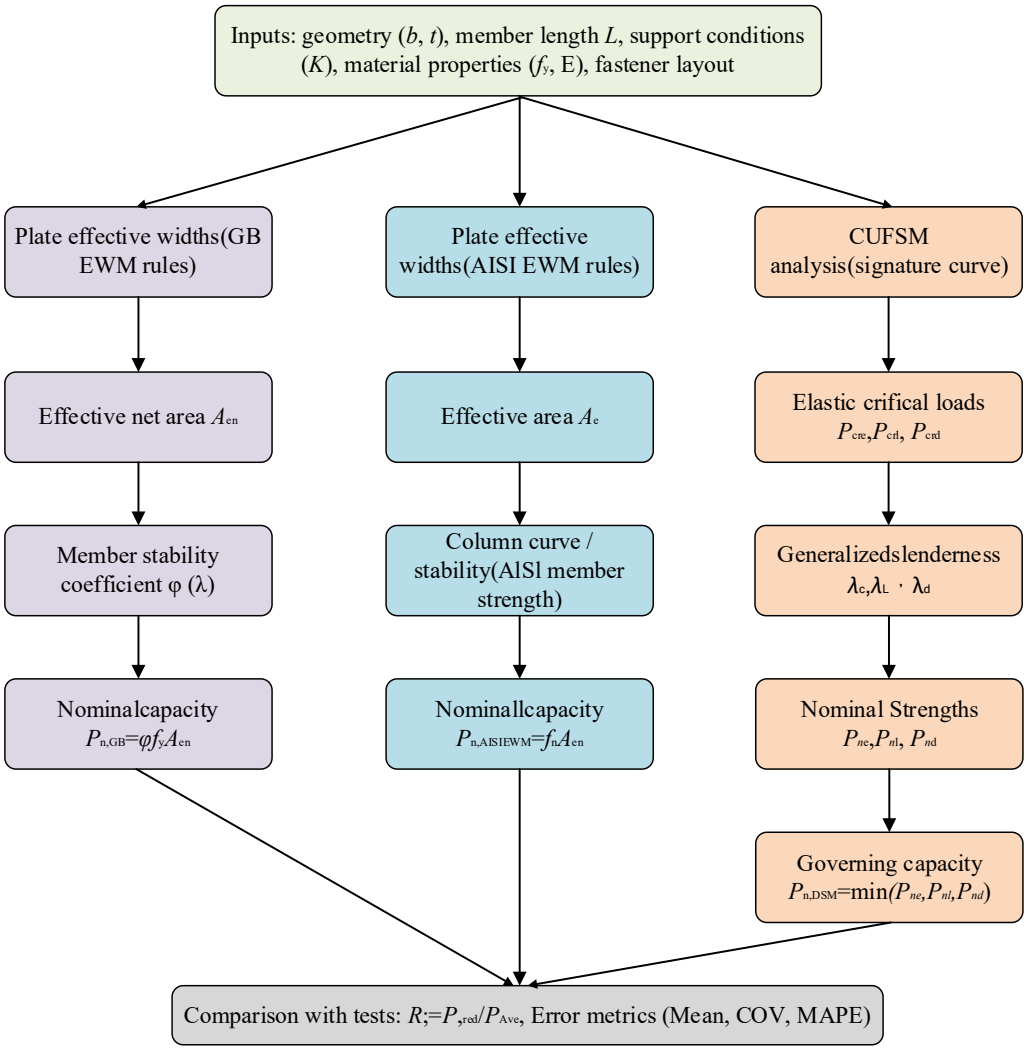

Fig. 13 Workflow of three code-based design paths.

4.1 Direct Strength Method (DSM, United States)

For clarity, the symbols used in the code-based calculations are defined as follows. The member slenderness ratio is $\lambda = KL/r_{min}$ (see Section 3), where L is the member length, K is the effective length factor (K =1.0 for the pin-ended conditions provided by the double knife-edge hinges), and r_{min} is the minimum radius of gyration of the gross cross-section. In the Direct Strength Method (DSM), $P_y = A_g f_y$ is the squash load, P_{cre} is the elastic critical global (overall) buckling load, and the reduced global slenderness is $\lambda_c = \sqrt{P_y/P_{cre}}$. The nominal global buckling strength P_{ne} is calculated from Eqs. (3a)–(3b).

The elastic critical buckling loads for local and distortional buckling are denoted P_{cr} and $P_{cr,d}$, respectively. In this study, P_{cre}, P_{cr} and $P_{cr,d}$ was obtained from an elastic buckling analysis using the CUFSM finite strip method based on the gross cross-section dimensions and the specimen length under simply supported (pin-ended) boundary conditions. A signature curve was generated by sweeping the half-wavelength from a small value up to the member length L; the minima corresponding to local (L), distortional (D) and global (G) modes were identified and taken as P_{cr}, $P_{cr,d}$ and $P_{cr,e}$. The reduced local and distortional slenderness parameters are defined as $\lambda_l = \sqrt{P_y/P_{cr}}$ and $\lambda_d = \sqrt{P_y/P_{cr,d}}$, and the corresponding nominal strengths P_{nl} and P_{nd} are calculated from Eqs. (5a)–(5b) and (6a)–(6b), respectively.

In the CUFSM analyses, the gross cross-section geometry was used. For built-up sections, the connected limbs were modelled as a fully composite (monolithic) section, which is consistent with the design assumption adopted by AISI S100 when screw spacing satisfies the connection detailing requirements. The global buckling load P_{cre} was taken as the minimum in the long half-wavelength region (≈member length), P_{crl} was taken as the minimum in the short half-wavelength (local) region, and P_{crd} was taken as the intermediate-wavelength minimum associated with distortional deformations of the stiffened elements.

In the AISI specification, the DSM provisions for cold-formed steel compression members are adopted, and the nominal axial strength is calculated as follows [21]:

$$P_n = \min(P_{ne}, P_{nl}, P_{nd}), \ \lambda_c < 1.5 \tag{3a}$$

$$P_{ne} = (\frac{0.877}{\lambda_c^2})P_y, \ \lambda_c > 1.5 \tag{3b}$$

$$\lambda_c = \sqrt{P_y / P_{cre}} \tag{4}$$

Yield capacity: $P_y = A_g f_y$

where A_g is the gross cross-sectional area, and f_y is the yield stress. The critical buckling load P_{cre} is obtained through buckling analysis using finite element or finite strip methods. Local buckling is calculated as

$$P_{nl} = P_{ne}, \ \lambda_l \leq 0.776 \tag{5a}$$

$$P_{nl} = (1\text{-}0.15(\frac{P_{crl}}{P_{ne}})^{0.4}(\frac{P_{crl}}{P_{ne}})^{0.4}P_{ne}, \ \lambda_l > 0.776 \tag{5b}$$

Note that P_{ne}, P_{nl}, and P_{nd} are DSM nominal strengths rather than elastic critical loads. In this study, the elastic critical loads (P_{cre}, P_{crl}, and P_{crd}) were first obtained from CUFSM as described above, and the DSM nominal strengths were then calculated using the AISI S100-2007 compression-member expressions. The design strength for each specimen was finally taken as P_n = min(P_{ne}, P_{nl}, P_{nd}).

Treatment of mode interaction in DSM: Following AISI S100-2007 [21], the DSM column provisions evaluate global (overall), local, and distortional buckling through separate nominal strengths (P_{ne}, P_{nl}, and P_{nd}). Local–global interaction is implicitly considered because P_{nl} is expressed as a function of P_{ne} and the local critical load P_{crl}, while distortional buckling is evaluated independently using P_{crd}. Therefore, combined L–G–D interactions are not explicitly superposed; instead, the controlling mode is taken as the minimum among {P_{ne}, P_{nl}, P_{nd}}. This approach is consistent with DSM practice and provides a conservative envelope when more than one instability pattern is evident in the tests. The implications of possible interaction effects beyond the standard DSM provisions are further discussed in Section 4.4. The equation is computed as

$$P_{nd} = P_{ne}, \ \lambda_d \leq 0.776 \tag{6a}$$

$$P_{nl} - (1 - 0.15(\frac{P_{crl}}{P_{ne}})^{0.4}(\frac{P_{crl}}{P_{ne}})^{0.4} P_{ne}, \ \lambda_{\mathrm{d}} > 0.776 \tag{6b}$$

$$\lambda_d = \sqrt{P_y / P_{crd}} \tag{7}$$

All three types of critical buckling stresses—P_{ne}, P_{nl}, and P_{nd}—are obtained through computational analysis using the CUFSM finite strip software.

4.2 Effective Width Method (EWM, United States)

Using extensive experimental data that considered initial imperfections and element stiffening, Winter [22] derived the following effective-width formula, which forms the basis of the Effective Width Method adopted in major cold-formed steel design standards, such as AISI S100-2007 [21] and GB 50018-2002 [23]. To avoid ambiguity, in this subsection λ denotes the reduced plate slenderness ratio used in the EWM, which is defined as:

$$\lambda = \sqrt{\frac{f}{\sigma_{cr}}} \tag{8}$$

The elastic critical buckling stress of a plate element is

$$\sigma_{cr} = k \frac{\pi^2 E}{12(1-\nu^2)} \left(\frac{t}{b} \right)^2 \tag{9}$$

where b is the flat width of the plate element, t is the thickness, E is the Young's modulus, v is Poisson's ratio, and k is the elastic buckling coefficient (K = 4.0 for a uniformly compressed stiffened element). The effective width is then calculated as $b_{\mathrm{e}} = \rho_{\mathrm{b}}$, and the effective cross-sectional area A_{e} is obtained by summing the effective areas of the constituent plate elements. The American specification stipulates that the axial compressive capacity of members shall be calculated using the following expression:

For the EWM calculations, each plate element (web, flange, and lip) was treated using the AISI S100 effective-width rules, where the elastic plate buckling stress is calculated as:

$$f_{cr} = \frac{k\pi^2 E}{12\left(1-\nu^2\right)} \left(\frac{t}{b} \right)^2 \tag{10}$$

The reduced plate slenderness is defined as $\lambda = \sqrt{F_y / f_{cr}}$, and the effective width be is computed using the corresponding reduction factor ρ (Eqs. (12)). The effective area A_{e} was obtained by summing the effective widths multiplied by thickness (corner radii were neglected for consistency with the code idealization). The nominal compressive stress F_{n} was then calculated by the AISI column curve using F_{e}, taken as the minimum elastic flexural, torsional, and flexural–torsional buckling stresses per AISI S100-2007.

$$P_n = A_e F_n \tag{11}$$

Calculation of the effective cross-sectional area A_{e}:

$$b_{\mathrm{e}} = b \ , \ \lambda \le 0.673 \tag{12a}$$

$$b_e = \rho b,\ \lambda > 0.673 \tag{12b}$$

$$\lambda = \sqrt{\frac{f}{\sigma_{cr}}} = \frac{1.052(b/t)}{\sqrt{k}}\sqrt{\frac{f}{E}} \tag{13}$$

where

$$\rho = \frac{1-0.22\rho}{\lambda} \tag{14}$$

where, b denotes the plate width, λ represents the reduced slenderness ratio, ρ is the reduction factor, E is the elastic modulus, and k is the elastic buckling coefficient, taken as 4.0.

The stress is calculated as:

$$F_n = (0.658^{\lambda_c^2}) f_y,\ \lambda_c < 1.5 \tag{15a}$$

$$F_n = (\frac{0.877}{\lambda_c^2}) f_y,\ \lambda_c > 1.5 \tag{15b}$$

where

$$\lambda_c = \sqrt{F_y / F_e} \tag{16}$$

where, F_y is the yield stress, and F_e is taken as the minimum value among the flexural buckling stress, torsional buckling stress, and flexural–torsional buckling stress.

4.3 Effective Width Method (China)

In the Chinese specification GB 50018-2002 [23], the axial compressive capacity of members is calculated using the following formulas:

Strength-based calculation:

$$N = A_{en} f_y \tag{17}$$

where A_{en} is the effective net cross-sectional area, and f_y is the yield strength of the material.

Stability-based calculation:

$$N = \varphi A_e f_y \tag{18}$$

In these expressions, A_{en} denotes the effective net cross-sectional area, and A_e denotes the effective gross cross-sectional area. The calculation of A_e depends on the boundary condition of each compressed plate element—categorized as stiffened, partially stiffened, or unstiffened. The effective areas of the flange, web, and lip are evaluated separately according to their respective conditions and then summed to obtain the total effective area. The formulas are as follows:

$$b_e = b,\ b/t \le 18\alpha\rho \tag{19}$$

$$b_e = (\sqrt{\frac{21.8\alpha\varphi}{b/t}} - 0.1)b,\ 18\alpha\rho < b/t \le 30\alpha\rho \tag{20}$$

$$b_e = \frac{18\alpha\rho}{b/t}b,\ b/t \ge 30\alpha\rho \tag{21}$$

where b is the plate width, α is a coefficient taken as $1.15-0.15\varphi$; φ is the edge-stress ratio for the compressed plate element, obtained by comparing the maximum compressive stress with the stress at the opposite edge (i.e., the stress at the less-compressed edge divided by the maximum compressive stress). The reduction factor ρ is given by：

$$\rho = \sqrt{\frac{205k_1k}{\sigma_1}} \tag{22}$$

where k_1 is the panel-group restraint factor, k is the plate buckling coefficient (adjusted according to whether the element is stiffened, partially stiffened, or unstiffened), and σ_1 is the reference stress.

When a built-up section is treated as a single (monolithic) section in calculations, the variation in slenderness is considered, but the mutual restraint among individual plate elements is not. Moreover, evaluating slenderness for the built-up member as a single section tends to overestimate the effectiveness of the connections between the constituent limbs.

4.4 Comparative Analysis of Code-Based Predictions

The load–slenderness curves for the six cross-section types, as obtained from the three calculation methods, are shown in Fig. 13. In these plots, P_u denotes the measured test capacity, P_{Ave} is the average of repeated tests for the same specimen, P_1 is the value predicted by the U.S. Effective Width Method, P_2 by the U.S. Direct Strength Method, and P_3 by the Chinese Effective Width Method. For single-limb members with $\lambda > 100$, the American provisions give relatively reasonable predictions, whereas all three methods tend to overestimate capacities when $\lambda < 100$. For built-up sections, the Chinese Effective Width Method (P_3) generally shows the closest overall agreement with the test results. In the global-buckling-dominated range (higher slenderness ratios), the Direct Strength Method (P_2) becomes noticeably more conservative, particularly for the C3U specimens, as illustrated in Fig. 13(f).

The load–slenderness curves for the six cross-section types, as obtained from the three calculation methods, are shown in Fig. 14. Here, P_{u} denotes the measured test capacity, P-A_{ve} is the average of repeated test results for the same specimen, P_1 is the value predicted by the U.S. Effective Width Method, P_2 by the U.S. Direct Strength Method, and P_3 by the Chinese Effective Width Method. To avoid overgeneralization, the relative prediction performance of each method is assessed for the present test database using the prediction-to-test ratio $R = P_{\mathrm{pred}}/P_u$ where values closer to unity indicate closer agreement.

As observed from Fig. 14(c)–(f), P_3 generally tracks the experimental data of the built-up sections (CU, CC, C2U2 and C3U) more closely over the investigated slenderness range, whereas the DSM predictions (P_2) tend to become increasingly conservative in the global-buckling-dominated range (higher $\boldsymbol{\lambda}$), as exemplified by the C3U section in Fig. 14(f). For single-limb members, all three methods may overestimate capacities in the lower slenderness range, which is primarily associated with distortional/local buckling and the limitations of applying code formulations calibrated for different section/buckling characteristics; this limitation is highlighted herein when interpreting Fig. 14(a)–(b).

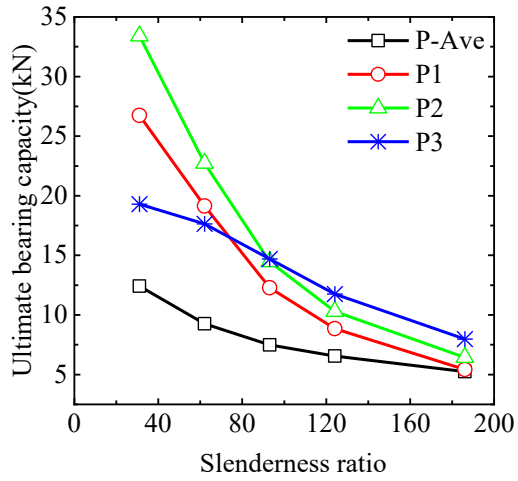

(a) U-section

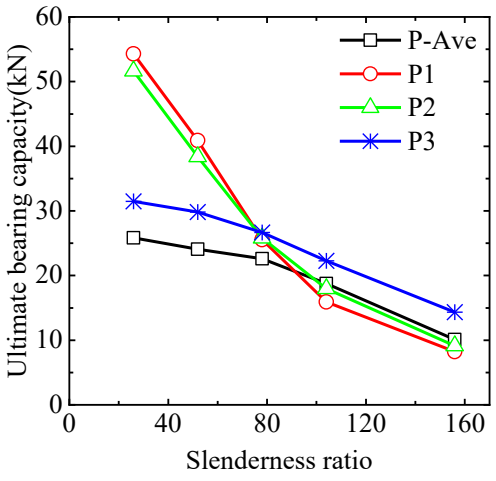

(b) C-section

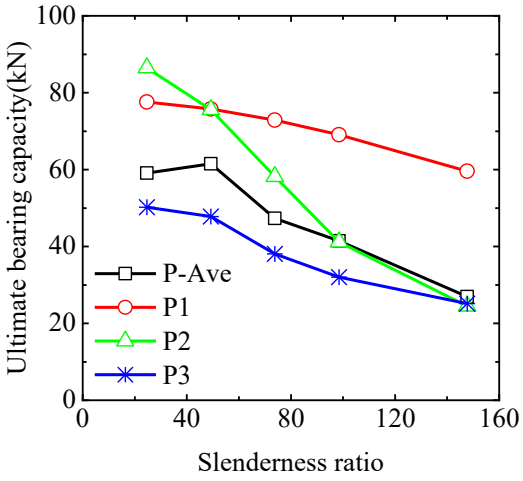

(c) CU-section

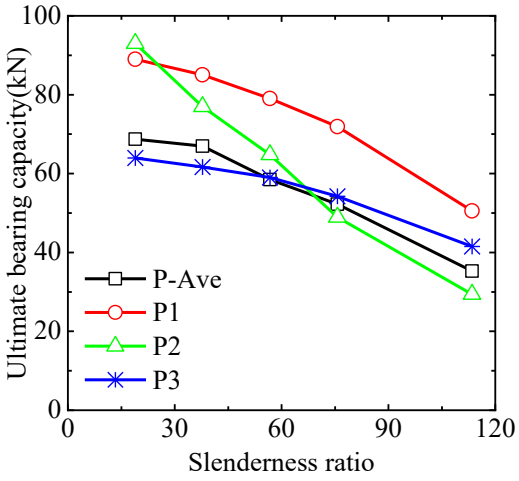

(d) CC-section

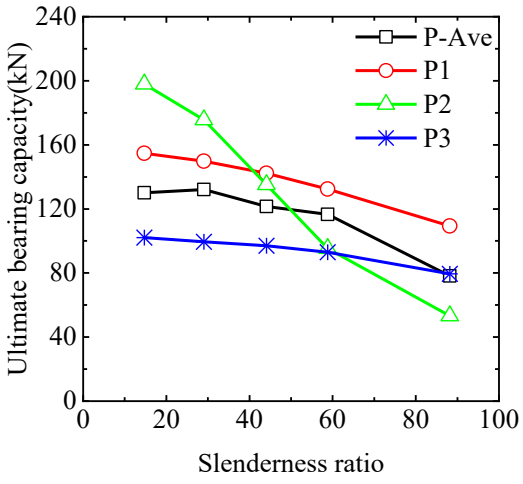

(e) C2U2-section

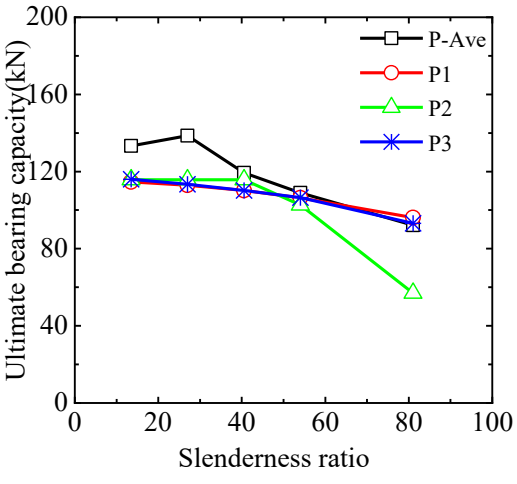

(f) C3U-section

Fig. 14 Load vs slenderness ratio curve

To quantify prediction accuracy, the prediction-to-test ratio is defined as $R = P_{\text{pred}}/P_{\text{Ave}}$. The bias (mean ratio) μ_R, coefficient of variation $COV_R = s_R/\mu_R$, and the mean absolute percentage error $MAPE = \frac{1}{n}\sum_{i=1}^{n} | R_i - 1 | \times 100\%$ are used to compare the three methods. The resulting statistics are summarized in Table 6 for built-up and single-limb members, respectively.

5. Stability Coefficients

By comparing the stability provisions for axially compressed members in AISC 360-05 (United States) [24], EN 1993 (Europe) [25], and China's GB 50018-2002 for cold-formed thin-walled steel [23], stability coefficients for the tested built-up sections were evaluated against these codes, from which the column curves for G550 steel were derived.

In the AISC 360-05 Specification (United States), the overall stability reduction factor φ is calculated using the following expressions:

$$\varphi = f_{cr} / f_y = 0.658^{\bar{\lambda}^{-2}},\ \bar{\lambda} \le 1.5 \tag{23}$$

$$\varphi = f_{cr} / f_y = 0.877 / \lambda^{-2},\ \bar{\lambda} > 1.5 \tag{24}$$

Where

$$\bar{\lambda} = \sqrt{\frac{Af_y}{N_{cr}}} = \sqrt{\frac{Af_y}{\pi^2 EA / \lambda^2}} = \frac{\lambda}{\pi}\sqrt{\frac{f_y}{E}} \tag{25}$$

In EN 1993 (Eurocode 3), column curves are classified into five types according to cross-section form, buckling about the strong/weak axis, and manufacturing process. The specimens in this study fall into curve *c*, for which the stability reduction factor is calculated as follows:

$$\varphi = 1.0,\ \bar{\lambda} \le 0.2 \tag{26}$$

$$\varphi = 1/\psi + \sqrt{\psi^2 - \bar{\lambda}^2},\ \bar{\lambda} \le 1.5 \tag{27}$$

$$\psi = 0.5[1 + \alpha(\bar{\lambda} - 0.2) + \bar{\lambda}^2] \tag{28}$$

For curve *c*, α =0.49. The Chinese code provides stability coefficient tables only for steels Q235 and Q345. The slenderness–stability coefficient curves from the three codes are compared with the Euler curve and the experimental results, as shown in Fig. 15.

Although both GB 50018-2002 and AISI S100-2007 adopt effective-width concepts, their member stability (column) curves and the manner in which effective section properties are coupled with stability reduction differ. For the present built-up database, the GB stability coefficient curve (curve c) yields reduction factors that are closer to the measured behavior of the closed multi-limb sections, which exhibited limited torsional–flexural coupling and lower imperfection sensitivity under the nominally pin-ended tests. In addition, the multi-limb assembly restrains local/distortional deformations, so the global response is governed primarily by flexural buckling, for which the GB stability curve provides a reasonable representation. By contrast, the AISI DSM evaluates global, local and distortional buckling through separate nominal strengths and adopts $P_n = \min(P_{ne}, P_{nl}, P_{nd})$, which may become conservative when the elastic local/distortional critical loads obtained from CUFSM remain low even though the built-up assembly delays the development of these modes in the tests. These interpretations are specific to the present specimen set and the connection detailing adopted herein.

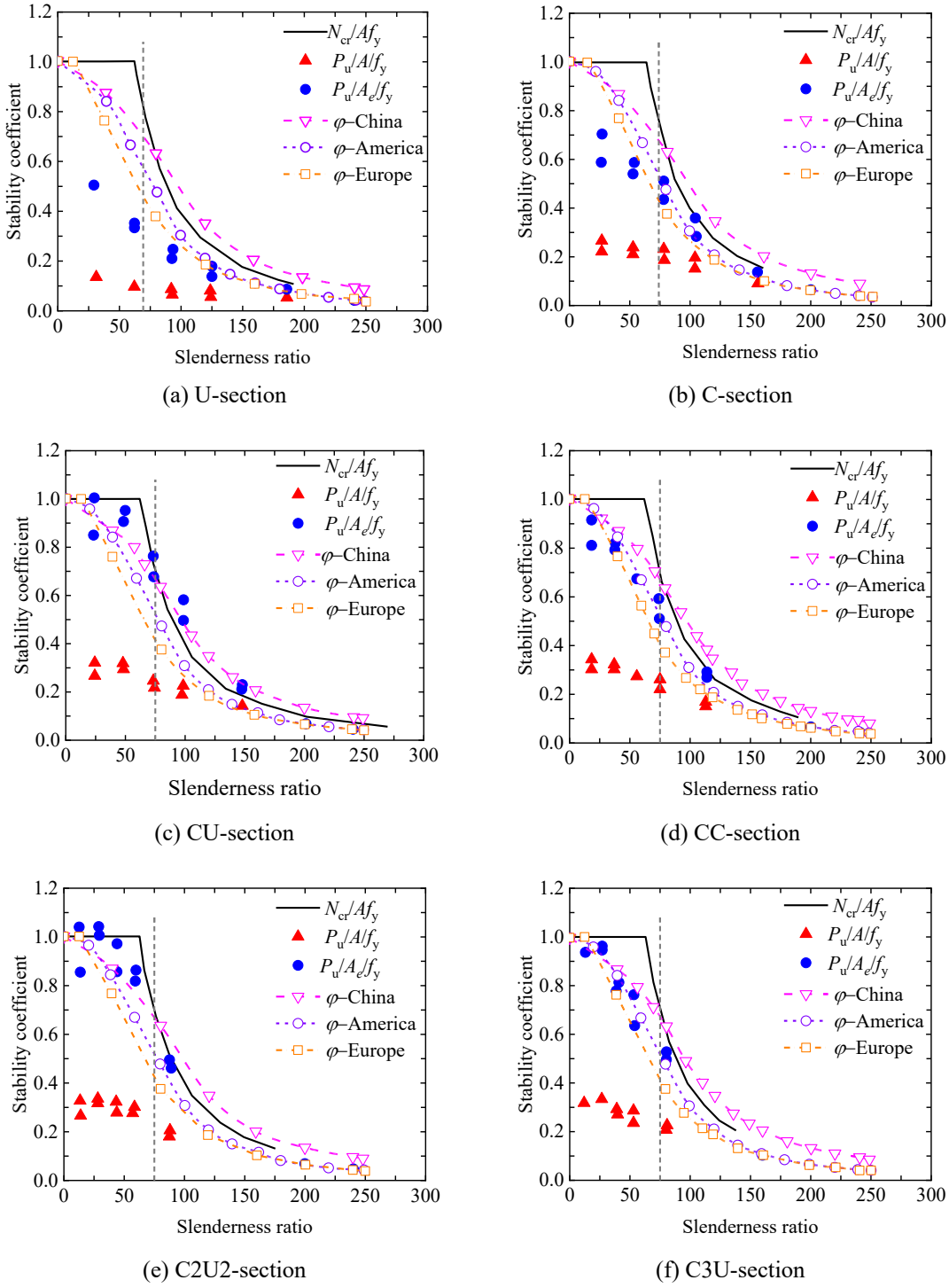

(a) U-section (b) C-section

(c) CU-section (d) CC-section

(e) C2U2-section (f) C3U-section

Fig. 15 Slenderness ratio vs stability coefficient curve

6. Built-Up Coefficient Stability Coefficients

According to the definition proposed by Liu Huiying [26], the built-up coefficient η is given by:

$$\eta=\frac{P_{u\text{Built-up section}}}{\sum P_{u\text{single-limb}}} \tag{29}$$

For the double-limb built-up sections (CU and CC), the built-up coefficient η in Eq. (29) can be interpreted as an interaction (or composite-action) factor between the two-constituent single-limb members, because the denominator represents the sum of their individual axial capacities. Using the present test database (Table 4), η ranges from 1.54 to 1.83 for the CU

sections (λ=24.62-147.73) and from 1.29 to 1.74 for the CC sections (λ=18.92-113.5), indicating significant mutual restraint provided by the discrete screw connections and the resulting increase in structural integrity compared with isolated single limbs. The interaction factor generally increases with member slenderness because the built-up assembly delays the transition to global buckling relative to the single-limb members; nevertheless, η is configuration- and connection-dependent, and further parametric studies on fastener spacing and detailing are needed to generalize an explicit interaction factor for design.

i.e., the ratio of the ultimate capacity of the built-up member to the sum of the ultimate capacities of its constituent single-limb members (see Fig. 15). As shown in Fig. 15, η increases with slenderness ratio, primarily because, at the same slenderness, four-limb sections tend to fail by distortional or local buckling. In contrast, the individual single-limb components within the built-up assembly have already transitioned to global buckling. The built-up Coefficient of four-limb sections exceeds that of double-limb sections; when the slenderness ratio exceeds 80, η for four-limb sections is approximately 1.5 times that for double-limb sections. This indicates a higher degree of structural integrity for four-limb configurations compared with double-limb ones, and likewise a greater integrity for closed sections compared with open sections.

Fig 16 compares the variation of η for the four built-up configurations. Cross-section geometry affects η through torsional rigidity, warping restraint and load-sharing between limbs. Closed multi-limb built-up sections (e.g., C2U2 and C3U) provide a closed shear-flow path and higher torsional stiffness, which suppresses distortional deformation and promotes a more uniform axial stress distribution; therefore, they tend to exhibit higher η than open double-limb sections (CU and CC) within the investigated range. The number and arrangement of limbs also change the effective radius of gyration and the sensitivity to overall flexural buckling, which influences the relative difference between built-up and single-limb capacities.

Connection density (screw spacing) provides the mechanical means for interaction by transferring shear and restraining relative slip; smaller spacing (Table 2) generally enhances composite action and can increase η. In this study, screw spacings were designed to satisfy code detailing limits, and the spacings were comparable for CU and CC and for C2U2 and C3U at a given length, suggesting that the observed differences in η among configurations are primarily driven by section closure and limb arrangement, while connection density acts as a secondary parameter within the investigated range. A targeted parametric study varying screw spacing and end margins is recommended to isolate the connection-density effect.

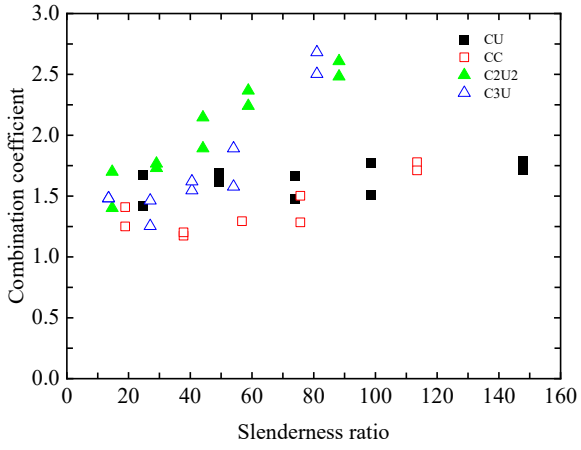

Fig. 16 The curve of the split coefficient and the slenderness ratio

7. Conclusions

Based on axial compression tests on cold-formed thin-walled steel single-limb and built-up sections, and comparison of the test results with predictions from three code-based methods, the following conclusions are drawn:

(1) For slenderness ratios $\lambda < 70$, closed built-up sections exhibit strong mutual restraint between constituent single limbs, leading to failure governed by local buckling rather than distortional buckling.

(2) For built-up sections with $\lambda > 80$, failure is governed by global buckling; in this regime, design may be based on the global critical buckling stress.

(3) The experimentally derived built-up Coefficient depends on the cross-sectional configuration and increases with increasing slenderness ratio.

(4) For built-up sections, the Chinese Effective Width Method generally provides the closest overall agreement with the test results, while the Direct Strength Method tends to yield more conservative predictions at higher slenderness ratios (global-buckling-dominated regime). For single-limb members, the Chinese Effective Width Method still overestimates the ultimate capacity by approximately 50%.

(5) For closed multi-limb built-up members within the investigated slenderness range and with the connection detailing satisfying the adopted screw-spacing limit, the GB 50018-2002 EWM provides relatively closer predictions for the built-up sections and can be used as a practical design approach. The AISI DSM generally yields conservative predictions and may be adopted as a lower-bound estimate, particularly at higher λ. For single-limb members, the Chinese EWM may be unconservative; therefore, AISI-based methods or calibrated reduction factors should be considered in design practice.

Future studies will extend the database to enable reliability-based resistance-factor calibration and to quantify the effects of screw spacing/connection density and intermediate stiffeners, measured initial imperfections, and combined actions such as cyclic loading and elevated-temperature/fire exposure.

Conflicts of Interest

The authors declare no conflict of interest.

References

[1] S. Selvaraj and M. Madhavan, "Structural Behaviour of Cold-Formed Steel Built-Up Closed Cross-section Columns - Assessing the Influence of Parameters and Design Methods," Engineering Structures, vol. 294, article no. 116600, 2023.

[2] S. F. Nie, M. R. Eatherton, Y. Han, and T. H. Zhou, "Investigation of Built-Up Box Columns Composed of Four Cold-Formed Steel Channels," Thin-Walled Structures, vol. 175, article no. 109258, 2022.

[3] M. S. Deepak and G. B. G. Ananthi, "Local Buckling Behaviour and Capacities of Cold-Formed Steel Double-I-Box Stub and Short Column Sections," Structures, vol. 34, pp. 1761-1784, 2021.

[4] J. J. Yang, L. Xu, Y. Shi, and W. Y. Wang, "Experimental and Analytical Study of Flexural Buckling of Cold-Formed Steel Quadruple-Limb Built-Up Box Columns," Journal of Structural Engineering, vol. 148, no. 1, article no. 04021228, 2022.

[5] L. Zhang, T. H. Zhou, L. R. Sang, Y. Z. Wang, and S. B. Wang, "Experiments on Local–Distortional Interaction Buckling of Cold-Formed Steel Three-Limbed Built-Up Open-Section Columns," Thin-Walled Structures, vol. 182, part A, article no. 110239, 2023.

[6] Y. C. Li, T. H. Zhou, A. H. Han, W. H. Li, and Y. Xu, "Failure Mechanism and Reliability Prediction of CFS Built-Up Columns Considering Distortional Buckling," Structures, vol. 69, article no. 107337, 2024.

[7] B. G. A. Gurupatham, K. Roy, G. M. Raftery, and J. B. P. Lim, "Influence of Intermediate Stiffeners on Axial Capacity of Thin-Walled Built-Up Open and Closed Channel Section Columns," Buildings, vol. 12, no. 8, article no. 1071, 2022.

[8] B. G. A. Gurupatham, K. Roy, and J. B. P. Lim, "Effect of Stiffeners on the Axial Strength of Face-to-Face Unequal-Angle Cold-Formed Steel Columns," Buildings, vol. 15, no. 1, article no. 88, 2025.

[9] G. B. G. Ananthi, K. Ghosh, K. Roy, A. Uzzaman, and J. B. P. Lim, "Tests, Modelling and Design of Unsymmetrical Back-to-Back Coldformed Steel Angles under Compression," Advanced Steel Construction, vol. 20, no. 2, pp. 188-198, 2024.

[10] W. Wang, K. Roy, H. Rezaeian, Z. Fang, and J. B. P. Lim, "Experimental and Numerical Investigation of Cold-Formed Steel Telescopic Studs under Compression," Journal of Constructional Steel Research, vol. 212, article no. 108279, 2024.

[11] G. B. G. Ananthi, M. S. Deepak, K. Roy, and J. B. P. Lim, "Behaviour and Strength of Back-to-Back Built-Up Cold-Formed Steel Unequal Angle Sections with Intermediate Stiffeners under Axial Compression," Steel and Composite Structures, vol. 42, no. 1, pp. 1-22, 2022.

[12] G. B. G. Ananthi, K. Roy, A. M. M. Ahmed, and J. B. P. Lim, "Non-Linear Behaviour and Design of Web Stiffened Battened Built-Up Stainless Steel Channel Sections under Axial Compression," Structures, vol. 30, pp. 477-494, 2021.

[13] K. Roy, B. Chen, Z. Fang, A. Uzzaman, X. Chen and J.B.P. Lim, "Local and Distortional Buckling Behaviour of Back-to-Back Built-Up Aluminium Alloy Channel Section Columns," Thin-Walled Structures, vol. 163, article no. 107713, 2021.

[14] A. M. Mahar, S. A. Jayachandran, and M. Mahendran, "Design of Cold-Formed Steel Built-Up Back-to-Back Columns Subject to Local-Flexural Interactive Buckling," Journal of Structural Engineering, vol. 149, no. 12, article no. 04023182, 2023.

[15] Y. Mei, Y. Cui, C. Ma, Y. Sun and A. Su, "Tests, Numerical Simulations and Design of G550 High Strength Cold-Formed Steel Lipped Channel Section Columns Failing by Interactive Buckling," Thin-Walled Structures, vol. 192, article no. 111172, 2023.

[16] K. Jiang and O. Zhao, "Stainless Steel Built-Up Section Stub Columns: Testing, Numerical Modelling and Design," Thin-Walled Structures, vol. 191, article no. 111070, 2023.

[17] C. Ma, K. Jiang, A. Su, O. Zhao, and L. Gardner, "S700 High-Strength Cold-Formed Steel Built-Up I-Section Stub Columns: Testing, Numerical Modelling and Design," Engineering Structures, vol. 334, article no. 120261, 2025.

[18] ISO 377:2017, Steel and Steel Products—Location and Preparation of Samples and Test Pieces for Mechanical Testing, International Organization for Standardization, Geneva, 2017.

[19] GB/T 2975-2018, Steel and Steel Products—Location and Preparation of Samples and Test Pieces for Mechanical Testing, Standardization Administration of China, Beijing, 2018.

[20] Cold-Formed Steel Engineers Institute, Strength of Cold-Formed Steel Jamb Stud-To-Track Connections, Research Report RP08-1, 2008.

[21] AISI S100-2007, North American Specification for the Design of Cold-Formed Steel Structural Members, American Iron and Steel Institute, Washington D.C., 2007.

[22] G. Winter, "The Strength of Thin Steel Compression Flanges," Transactions of the ASCE, vol. 112, pp. 527-554, 1947.

[23] GB 50018-2002, Technical Code of Cold-Formed Thin-Walled Steel Structures, China Planning Press, Beijing, pp. 1-36, 2002.

[24] AISC 360-05, Load and Resistance Factor Design Specification for Structural Steel Buildings, American Institute of Steel Construction, Chicago, 2005.

[25] EN 1993 Eurocode 3, Design of Steel Structures, Part 1-1: General Rules and Rules for Buildings, European Committee for Standardization, London, 2005.

[26] H. Liu, "Compression Tests and Theoretical Research of Open-Section Built-Up Cold-Formed Steel Stub Columns," Master's thesis, Chang'an University, Xi'an, China, 2016.